ROYAL SOCIETY OF CHEMISTRY

Check for updates

Insights from ion mobility-mass spectrometry, infrared spectroscopy, and molecular dynamics simulations on nicotinamide adenine dinucleotide structural dynamics: NAD+ *vs.* NADH†

Juan Camilo Molano-Arevalo, [ID] [a] Walter Gonzalez,[a] Kevin Jeanne Dit Fouque, [ID] [a] Jaroslava Miksovska,[ab] Philippe Maitre[c] and Francisco Fernandez-Lima [ID] *[ab]

Nicotinamide adenine dinucleotide (NAD) is found in all living cells where the oxidized (NAD+) and reduced (NADH) forms play important roles in many enzymatic reactions. However, little is known about NAD+ and NADH conformational changes and kinetics as a function of the cell environment. In the present work, an analytical workflow is utilized to study NAD+ and NADH dynamics as a function of the organic content in solution using fluorescence lifetime spectroscopy and in the gas-phase using trapped ion mobility spectrometry coupled to mass spectrometry (TIMS-MS) and infrared multiple photon dissociation (IRMPD) spectroscopy. NAD solution time decay studies showed a two-component distribution, assigned to changes from a "close" to "open" conformation with the increase of the organic content. NAD gas-phase studies using nESI-TIMS-MS displayed two ion mobility bands for NAD+ protonated and sodiated species, while four and two ion mobility bands were observed for NADH protonated and sodiated species, respectively. Changes in the mobility profiles were observed for NADH as a function of the starting solution conditions and the time after desolvation, while NAD+ profiles showed no dependence. IRMPD spectroscopy of NAD+ and NADH protonated species in the 800–1800 and 3200–3700 cm^{-1} spectral regions showed common and signature bands between the NAD forms. Candidate structures were proposed for NAD+ and NADH kinetically trapped intermediates of the protonated and sodiated species, based on their collision cross sections and IR profiles. Results showed that NAD+ and NADH species exist in open, stack, and closed conformations and that the driving force for conformational dynamics is hydrogen bonding of the N–H–O and O–H–O forms with ribose rings.

Introduction

Nicotinamide adenine dinucleotide (NAD) is a ubiquitous molecule found in all living cells. The structure of NAD consists

[a] *Department of Chemistry and Biochemistry, Florida International University, Miami, FL 33199, USA. E-mail: fernandf@fiu.edu*
[b] *Biomolecular Sciences Institute, Florida International University, Miami, FL 33199, USA*
[c] *Laboratoire de Chimie Physique, Université Paris Sud, UMR 8000 CNRS, 91405 Orsay Cedex, France*

of two nucleotides, ribose rings with adenine and nicotinamide, joined together by a diphosphate bond.[1] The oxidized (NAD+) and reduced (NADH) forms of NAD have important roles in cellular metabolism, functioning both as hydride-accepting and hydride-donating coenzymes in over 300 enzymatically catalyzed oxidation–reduction reactions, which control transcription and gene expression, DNA repair, regulation of energy metabolism, cell death, and aging.[2–13] Besides serving as a multipurpose coenzyme, NAD is also used as a substrate of NAD-dependent ligases, NAD-dependent oxidoreductases, poly(ADP-ribose) polymerase (PARP) and the NAD-dependent deacetylases of the Sir2p family.[7,10,14–18]

Numerous human diseases are linked to fluctuations in the ratio between NAD+ and NADH forms.[19] NAD is converted into NADH mostly in catabolic reactions including glycolysis and the tricarboxylic acid cycle.[20] This delicate balance between the levels of NAD+ and NADH forms plays an important role in regulating the intracellular redox state and is often considered as a readout of the metabolic state as it fluctuates in response to a change in metabolism.[21–25] The fluorescence emission of

This journal is © the Owner Societies 2018

Phys. Chem. Chem. Phys., 2018, **20**, 7043–7052 | 7043

NADH has been used extensively for the study of the redox status of tissues when the cofactor is bound to enzymes,[26–30] while the identification of free and bound NADH is challenging because the fluorescence decay times are on the sub-nanosecond timescale.[31] Several studies have been focused on the theoretical structural interrogation of both NAD^{+} and NADH. *Ab initio* calculations were used to evaluate the conformational preferences of the nicotinamide ring while NAD^{+} and NADH were bound to dependent dehydrogenases.[32] It was found that the redox potential of the cofactor is a function of the ribose orientation, where the glycosidic C–O bond of NAD^{+} is near the plane of the nicotinamide ring, while the glycosidic C–O bond of NADH is nearly perpendicular to the dihydronicotinamide ring. The parametrization of empirical force fields for the modelling of NAD was performed following the methodology used in the development of CHARMM22 all-hydrogen parameters for proteins, nucleic acids, and lipids.[33] Molecular dynamics simulations of NAD^{+} in the presence of different solvents showed the presence of folded and extended conformation.[34]

Recently, trapped ion mobility spectrometry (TIMS) was used successfully in combination with fluorescence time decay studies and molecular dynamics in order to characterize the conformational populations of flavin adenine dinucleotide in solution and in the gas-phase.[35] The combination of these techniques has proven to be a versatile and powerful analytical workflow in the study of intermediate and equilibrium structures of biomolecules.[35–38] A more recent development of analytical instrumentation integrating both ion mobility separation and optical spectroscopy, either in the infrared,[39,40] or UV-visible[41,42] regions, has been shown to be effective for providing structural information on mass-selected ions. Infrared free electron lasers (IR FEL) and optical parametric oscillator/amplifier (OPO/A) benchtop lasers provide access to a wide frequency range, which allow recording of vibrational spectra in the mid-infrared and in the X–H (X = C, N, O) stretching regions, respectively. This so-called action spectroscopy has been particularly successful for distinguishing isomers[43,44] and unravelling the hydrogen bonding association with peptide structuration.[45,46]

In the present work, NAD^{+} and NADH forms were studied as a function of the solution organic content using fluorescence lifetime spectroscopy, TIMS-MS with collision induced activation (CIA), IRMPD spectroscopy and molecular dynamic simulations. Candidate structures were proposed for the kinetically trapped intermediates based on ion-neutral collision cross sections (CCS$_{N2}$), IRMPD spectroscopy, and molecular dynamic simulations. In particular, this study focuses on describing the differences in the intramolecular interactions of NAD^{+} and NADH.

Materials and methods

Materials and reagents

β-Nicotinamide adenine dinucleotide disodium salt hydrate (EC number 210-123-3) powder was purchased from Sigma-Aldrich (St. Louis, MO). All solvents and ammonium acetate salts were of analytical grade or better and purchased from Fisher Scientific (Pittsburg, PA). Stock solution was prepared in 10 mM ammonium acetate (pH 7.0) and aliquots were diluted to a final concentration of 10 μM in 100 : 00 to 50 : 50 (v/v) water–methanol/ethanol solutions in stepwise increments of 10% organic content. A Tuning Mix calibration standard (TuneMix, G24221A) was purchased from Agilent Technologies (Santa Clara, CA). Details on the Tuning Mix structures (*e.g.*, *m/z* 322 K_0 = 1.376 cm^2 V^{-1} s^{-1} and *m/z* 622 K_0 = 1.013 cm^2 V^{-1} s^{-1}) can be found elsewhere.[47,48]

NanoESI-CIA-TIMS-MS analysis

Ion mobility experiments were performed on a custom built nanoESI-TIMS coupled to a maXis Impact Q-ToF mass spectrometer (Bruker Daltonics Inc., MA). A 10 μL aliquot of the sample solution was loaded in the pulled-tip capillary and sprayed at 600–1200 V. Details regarding the TIMS operation and specifics compared to traditional IMS can be found elsewhere (the TIMS cell schematics can be found in Fig. S1, ESI†).[48–50] Briefly, TIMS ion mobility separation is based on holding the ions stationary using an electric field against a moving gas. The separation in a TIMS device can be described in the center of mass frame using the same principles as in a conventional IMS drift tube.[51] Since ion mobility separation is related to the number of ion-neutral collisions (or drift time in traditional drift tube cells), the ion mobility separation in a TIMS device depends on the bath gas drift velocity, ion confinement and ion elution parameters. The mobility, *K*, of an ion in a TIMS cell is described as

$$K = \frac{v_g}{E} \approx \frac{A}{(V_{elution} - V_{out})} \quad (1)$$

where v_g, E, $V_{elution}$ and V_{out} are the velocity of the gas, applied electric field, elution and last electrode voltages, respectively. The constant *A* can be determined using calibration standards of known mobilities. In TIMS operation, multiple isomers/conformers are trapped simultaneously at different *E* values resulting from a voltage gradient applied across the IMS tunnel region. After thermalization, isomers/conformers are eluted by decreasing the electric field in stepwise decrements (referred to as the "ramp"). Each isomer/conformer eluting from the TIMS cell can be described by a characteristic voltage ($V_{elution}$). In a TIMS device, the total analysis time (t_{Total}) can be described as

$$t_T = t_{trap} + \left(\frac{V_{elution}}{V_{ramp}}\right)t_{ramp} + tof = t_o + \left(\frac{V_{elution}}{V_{ramp}}\right)t_{ramp} \quad (2)$$

where t_{trap} is the thermalization/trapping time, tof is the time after the ion mobility separation, and V_{ramp} and t_{ramp} are the voltage range and time required to vary the electric field, respectively.[37,38] The elution voltage can be experimentally determined by varying the ramp time for a constant ramp voltage range.

The TIMS funnel is controlled using in-house software, written in National Instruments Lab VIEW, and synchronized with the maXis Impact Q-ToF acquisition program.[49,50] TIMS separation was performed using nitrogen as a bath gas at *ca.* 300 K, and the gas flow velocity was controlled by the pressure difference between the entrance funnel P_1 = 2.6 mbar, and the

7044 | *Phys. Chem. Chem. Phys.*, 2018, **20**, 7043–7052

This journal is © the Owner Societies 2018

exit funnel P_2 = 1.0 mbar. P_1 and P_2 values were kept constant for all experiments. The same rf (880 kHz and 200 V_{pp}) was applied to all electrodes including the entrance funnel, the ion mobility separating section, and the exit funnel. The TIMS cell was operated using a fill/trap/ramp/wait sequence of 10/10/100–500/50 ms.[49,50]

Mobility values (K) were correlated with CCS (Ω) using the equation:

$$\Omega = \frac{(18\pi)^{1/2}}{16} \frac{z}{(k_B T)^{1/2}} \left(\frac{1}{m_I} + \frac{1}{m_b}\right)^{1/2} \frac{1}{K} \frac{760}{P} \frac{T}{273.15} \frac{1}{N^*} \quad (3)$$

where z is the charge of the ion, k_B is the Boltzmann constant, N^* is the number density of the bath gas and m_I and m_b refer to the masses of the ion and the bath gas, respectively.[51] All resolving power (R) values reported herein were determined from Gaussian peak fits of the features in the TIMS distributions ($R = \Omega/\Delta\Omega$) using OriginPro (version 9.3.226). The FWHM of the mobility band was used to calculate the $\Delta\Omega$.

Collision induced activation (CIA) experiments were performed to assess the effect of the activation energy on the conformational space of NAD. Soft activation energy conditions were implemented to study the memory effect from the starting solution (capillary (V_{cap}): 50 V; deflector start (V_{def}): 60 V; entrance funnel (V_{fun}): 0 V). For CIA experiments, the energy conditions were increased by increasing the voltage of each region by 10 V (V_{cap}: 190 V; V_{def}: 200 V; V_{fun}: 150 V). A total of 500 accumulations and 10 frames were acquired per ramp time (*e.g.*, T_{ramp} = 100–500 ms).

Photo-physical characterization of NADH in solution

All fluorescence measurements were conducted using a PC1-ChronosFD custom instrument (ISS, Champaign Illinois). NAD was used without further purification and diluted from powder maintained at −20 °C into 10 mM ammonium acetate buffer at pH 8 and 100 μM concentration, and ethanol or methanol was added in the desired v/v ratio. All measurements were conducted at a room temperature of ∼18 °C. Steady-state emission spectra were obtained by exciting the sample with 350 ± 4 nm light along the 2 mm path of a 2 × 10 mm quartz cuvette, and the emission was collected through a vertical polarizer with an emission bandwidth of ±4 nm. Fluorescence and anisotropy decay experiments were performed in the frequency domain mode. NADH solutions were excited using a 370 nm intensity modulated laser diode and fluorescent emission was collected using a 400 nm long pass filter (Andover, Salem, NH). A solution of POPOP (1,4-bis(5-phenyloxazol-2-yl)benzene) in ethanol was used as a lifetime reference. Polarizers were set at the magic angle configuration for the lifetime measurements.[52] Modulation-phase data were analyzed using GlobalsWE software (Laboratory of Fluorescence Dynamics, Irvine, CA)[53] and the χ^2 parameter was used as a criterion for goodness of fit.[54]

ESI-FT-ICR MS-IRMPD analysis

Mass spectrometry and infrared action spectroscopy experiments were carried out employing a 7 T Fourier transform ion cyclotron resonance (FT-ICR) mass spectrometer (Apex Qe, Bruker) coupled with tunable infrared lasers at the CLIO facility (Orsay, France). A detailed layout of this experimental apparatus is described elsewhere.[55] Mass-selected ions were accumulated in an argon pressurized linear hexapole ion trap. Ions were then pulse extracted and stored in the ICR cell where they were irradiated with infrared light. Infrared action spectroscopy was carried out by monitoring the intensities of the precursor ($I_{precursor}$) and the resulting fragment ions ($I_{fragment}$) as a function of the laser wavenumber. The infrared action spectra were obtained by plotting the photo-dissociation efficiencies, defined as ln $(1 + \sum I_{fragment}/I_{precursor})$, as a function of the laser wavenumber. The infrared action spectra of NAD$^+$ and NADH were recorded in the 3200–3700 cm^{-1} spectral range using an optical parametric oscillator/amplifier (OPO/A from Laser Vision, Bellevue, WA) benchtop laser.[56] The irradiation time was 1 s. In order to enhance the infrared induced fragmentation efficiency, an auxiliary broadband CO$_2$ laser (BFI Optilas, Evry, France) was used.[57] The CO$_2$ pulse length was 500 μs for both NAD$^+$ and NADH. Infrared spectroscopy in the 800–1800 cm^{-1} spectral range was performed using the free electron laser (FEL, from CLIO, Orsay, France).[58] The irradiation time was set to 700 ms for both NAD$^+$ and NADH to record vibrational spectra in the mid-infrared region.

Theoretical calculations

A pool of candidate structures was proposed for the IMS bands observed in the nESI-TIMS-MS experiments. Briefly, consecutive molecular dynamic simulations were used to reproduce the experimental conditions (*e.g.* "TIMS" thermostat). In order to generate the initial pool of structures that populate the conformational space, the simulations were run at different temperature settings (*e.g.* 300–2500 K, with 100 K increases). This approach is equivalent to that previously described by Fernández-Lima and co-workers.[59] Molecular dynamics simulations of annealing and geometry optimization cycles were carried out in a *NVT* thermostat using the AMBER03[60] force field in YASARA software.[61] Every simulation was run for 10 ns and 400 snapshots per simulation were obtained. Final structures were optimized at the DFT/B3LYP/6-31G* level using Jaguar (Schrödinger, LLC, Cambridge, MA).[62] Vibrational frequencies were calculated and scaled by 0.961, according to the Computational Chemistry Comparison and Benchmark DataBase NIST.[63] Zero-point energy corrections were applied to the relative stability analysis between the structures. Theoretical ion-neutral collision cross sections were calculated using MOBCAL version for helium,[64,65] nitrogen,[66] and the software package IMoS.[67,68] Partial atomic charges were calculated using the Merz–Singh–Kollman scheme constrained to the molecular dipole moment.[69,70]

Results and discussion

nESI-TIMS-MS analysis of NAD showed protonated and sodiated molecular ions (Fig. 1). The most abundant [M + H]$^+$ and [M + Na]$^+$ ions correspond to the reduced form, NADH (M = $C_{21}H_{29}N_7O_{14}P_2$),
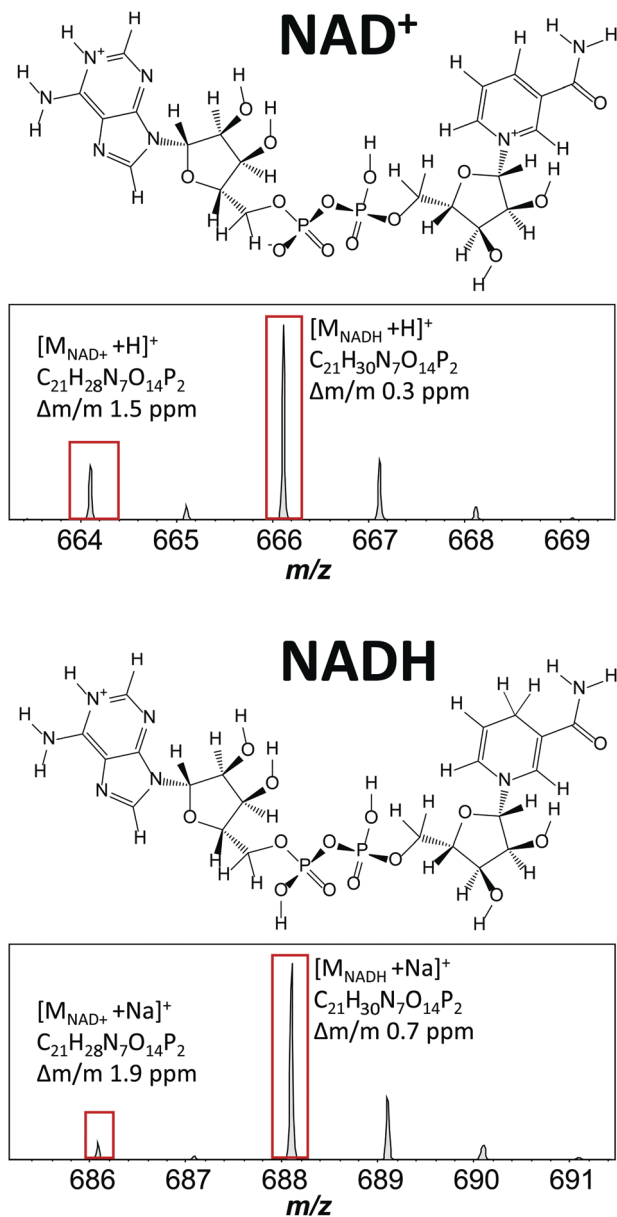
This journal is © the Owner Societies 2018

Phys. Chem. Chem. Phys., 2018, **20**, 7043–7052 | 7045

Fig. 1 Structures of the oxidized (M = $C_{21}H_{27}N_7O_{14}P_2$) and reduced (M = $C_{21}H_{29}N_7O_{14}P_2$) NAD forms. Typical MS spectra of protonated and sodiated molecular ions of both NAD species are shown.

Fig. 2 Ion mobility profiles of NAD (t_{trap} = 500 ms) as a function of the organic content in the starting solution (blue panel) and the collision induced activation energy (red panel). Labels A–D are assigned to the IMS bands of the NADH $[M + H]^+$ species; E and F to NADH $[M + Na]^+$ species; G and H to NAD$^+$ $[M + H]^+$ species; and I and J to NAD$^+$ $[M + Na]^+$ species.

while similar molecular ions were observed for the oxidized form, NAD$^+$ (M = $C_{21}H_{27}N_7O_{14}P_2$).

Different starting solvent conditions were considered to simulate potential differences in the cell environment of NAD, which could lead to rearrangements in the conformational space (e.g., high/low organic). That is, nESI-TIMS-MS as a function of the organic content in solution (e.g. 0–50 mM NH$_4$Ac, 0–50% MeOH or EtOH) and activation energy (CIA-TIMS-MS) showed multiple IMS bands for the protonated and sodiated species of NAD$^+$ and NADH (labels A–J in Fig. 2). Inspection of the ion mobility profile for $[M_{NADH} + H]^+$ showed four mobility bands (labels A–D) for all starting solutions. Moreover, the relative abundance of B was greater when the solution contained NH$_4$Ac
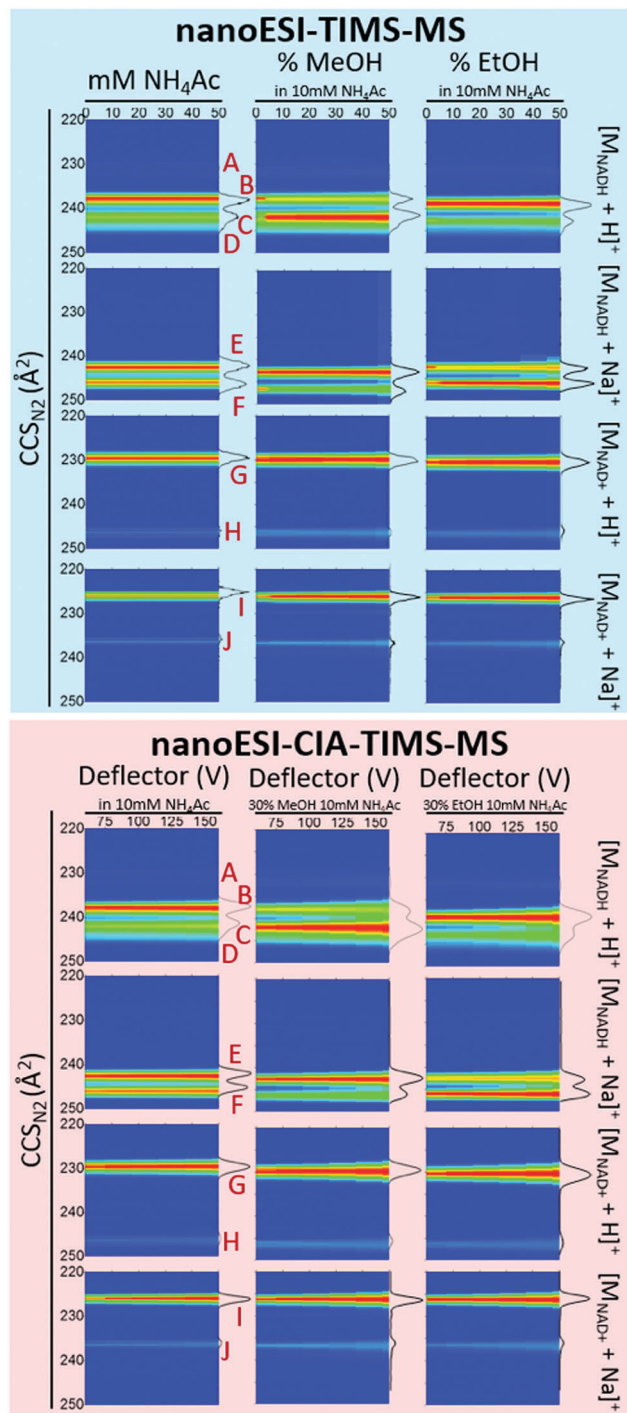
or EtOH, while C was more abundant when MeOH was added to the starting solution. For $[M_{NADH} + Na]^+$ (labels E and F), the intensity of E was slightly greater than F in the NH$_4$Ac solution, considerably greater when MeOH was added, and smaller than F when EtOH was added. These changes in the

7046 | *Phys. Chem. Chem. Phys.*, 2018, **20**, 7043–7052

This journal is © the Owner Societies 2018

relative abundances of the mobility bands suggest that, at the molecular level in solution, the interaction with the organic molecules drives the equilibria between the multiple conformations. Major differences in the relative abundances of the ion mobility profiles for $[M_{NAD^+} + H]^+$ (labels G and H), and $[M_{NAD^+} + Na]^+$ (labels I and J) were not observed as a function of the starting solution conditions (Fig. 2) and the trapping time (*e.g.*; 100–500 ms, data not shown). This suggests that the species formed during the nanoESI process are stable in the TIMS-MS experiments time scale, and that the solvation effects of the organic molecules are not enough to favor conformational interconversion of the oxidized NAD. Moreover, no changes in the CCS_{N2} values were observed as a function of the organic content in the starting solutions, which suggests that the observed ion mobility bands correspond to different conformations of NAD and not to organic solvent clustering with the molecular ions in the gas-phase.

Further sampling of the conformational space of NAD in the gas phase was performed *via* collision induced activation (CIA) prior to the ion mobility separation (Fig. 2, red panel). While the same number of mobility bands were observed as a function of the CIA condition, some changes in the relative abundances of the mobility bands were observed; we interpret this variation as the interconversion between the most energetically favorable conformational populations. Moreover, population interconversion between NADH mobility bands was observed as a function of the trapping time (*e.g.*, 100–500 ms) and the organic content (*e.g.*, MeOH and EtOH) for the protonated and sodiated species (Fig. 3). Inspection of the mobility profiles showed a decrease (red pattern area under the curve) of B for $[M_{NADH} + H]^+$, favoring the increase (blue pattern area under the curve) in the abundance of C. Similarly, inspection of the profiles for $[M_{NADH} + Na]^+$ showed that the relative abundance of E increased while the abundance of the F mobility band decreased. These results suggested that kinetically trapped intermediates can interconvert into other local free energy minima after thermalization in the TIMS cell.[71] The effect of the nature of organic content on the conformational space was observed by changes in the starting relative abundance of the mobility bands, for example, B and C mobility bands for $[M_{NADH} + H]^+$ and E and F mobility bands for $[M_{NADH} + Na]^+$ showed different relative abundances with the starting solution organic content (MeOH *vs.* EtOH).

The heterogeneity of NAD in solution was characterized by measuring the NAD lifetime as a function of the organic content (*e.g.*, 10–70% methanol and ethanol) using frequency domain fluorescence spectroscopy (Fig. 4). The data were analyzed using a double exponential decay model and the results are summarized in Table S1 (ESI†). Two different components that can be attributed to different conformational groups were resolved: a fast decaying component of 0.3 ns, attributed to the intermediates with a "closed" conformation; and a slow component of 0.94 ns, attributed to the intermediates belonging to both "stack" and "open" conformations.[31] Inspection of Fig. 4 shows that a change in the solution dielectric constant with the organic content alters the fraction of the "stack" and "open" conformations. A comparison between methanol and ethanol showed fast
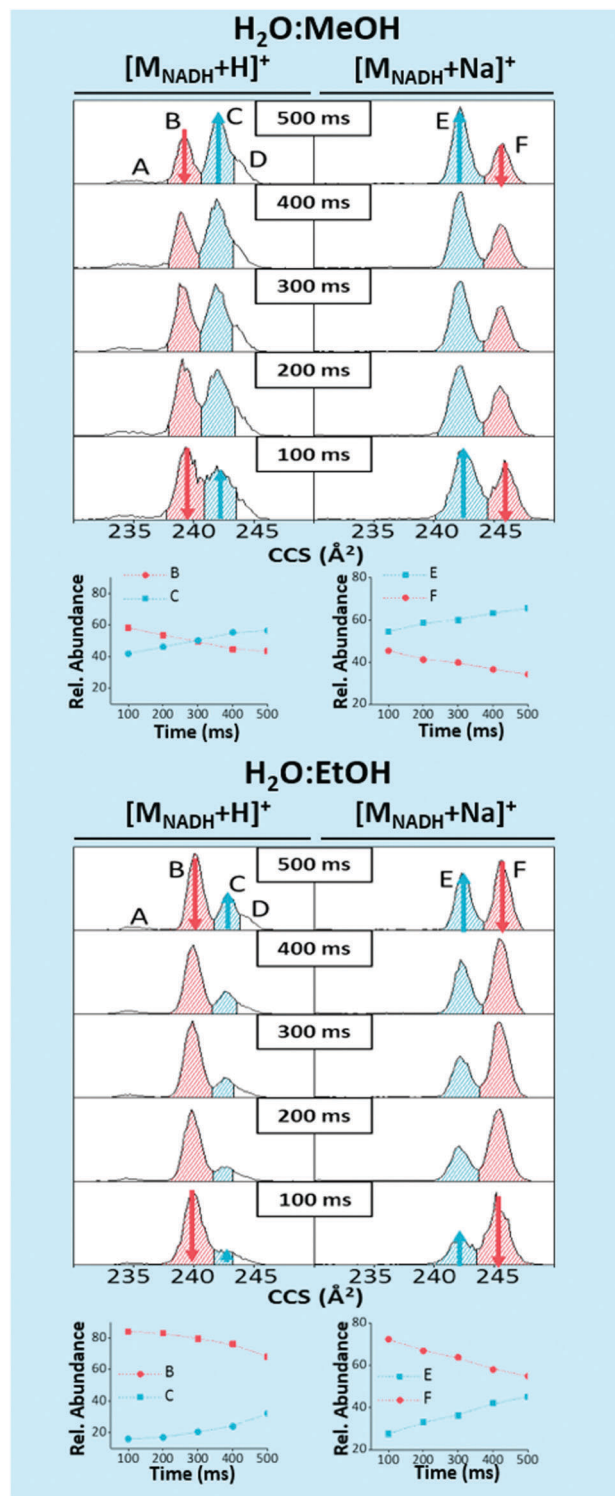

Fig. 3 Typical IMS and interconversion plots as a function of the trapping time and starting solvent conditions (70 : 30 H_2O : MeOH and H_2O : EtOH) for NADH $[M + H]^+$ and $[M + Na]^+$ species.

and slow decay times, but a faster change in the fast/slow ratio for ethanol when compared to methanol. These observations are in good agreement with the trends observed during the TIMS-MS analysis (*i.e.*, kinetic trapped intermediates, Fig. 3) and support
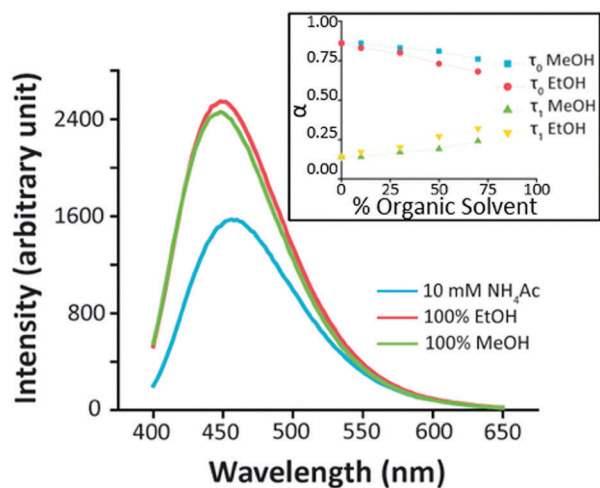
Fig. 4 Emission spectra of NAD as a function of the organic content. In the inset, changes in the pre-exponential factor (α) are shown as a function of organic content for the fast (τ_0) and slow (τ_1) components.

the hypothesis that "memory effects" of the starting solution can be retained in the mobility profiles using "soft" conditions in transmission settings in the TIMS-MS experiments.

Complementary studies of NAD$^+$ and NADH using IRMPD spectroscopy permitted the interrogation of the chemical local environment of the gas-phase ions (Fig. 5). A comparison of IR spectra of NAD$^+$ and NADH protonated species showed the presence of common as well as signature bands. A tentative assignment of the observed infrared bands and the atoms involved in the intramolecular interactions of the protonated species of NAD$^+$ and NADH is proposed in Tables S3 and S4 (ESI†). In the high energy range (e.g., 3300–3700 cm^{-1}), the bands observed at ~3660 cm^{-1} were present for both NADH and NAD$^+$ forms and were assigned to free phosphate OH stretches (Fig. 5).[72] The bands observed near ~3560 cm^{-1} are typical signatures of free NH$_2$ asymmetric stretches.[73] Two other common bands between NAD$^+$ and NADH were observed at ~3430 and ~3540 cm^{-1}, and could be tentatively assigned to N–H–O and O–H–O stretch interactions, respectively.[74,75]
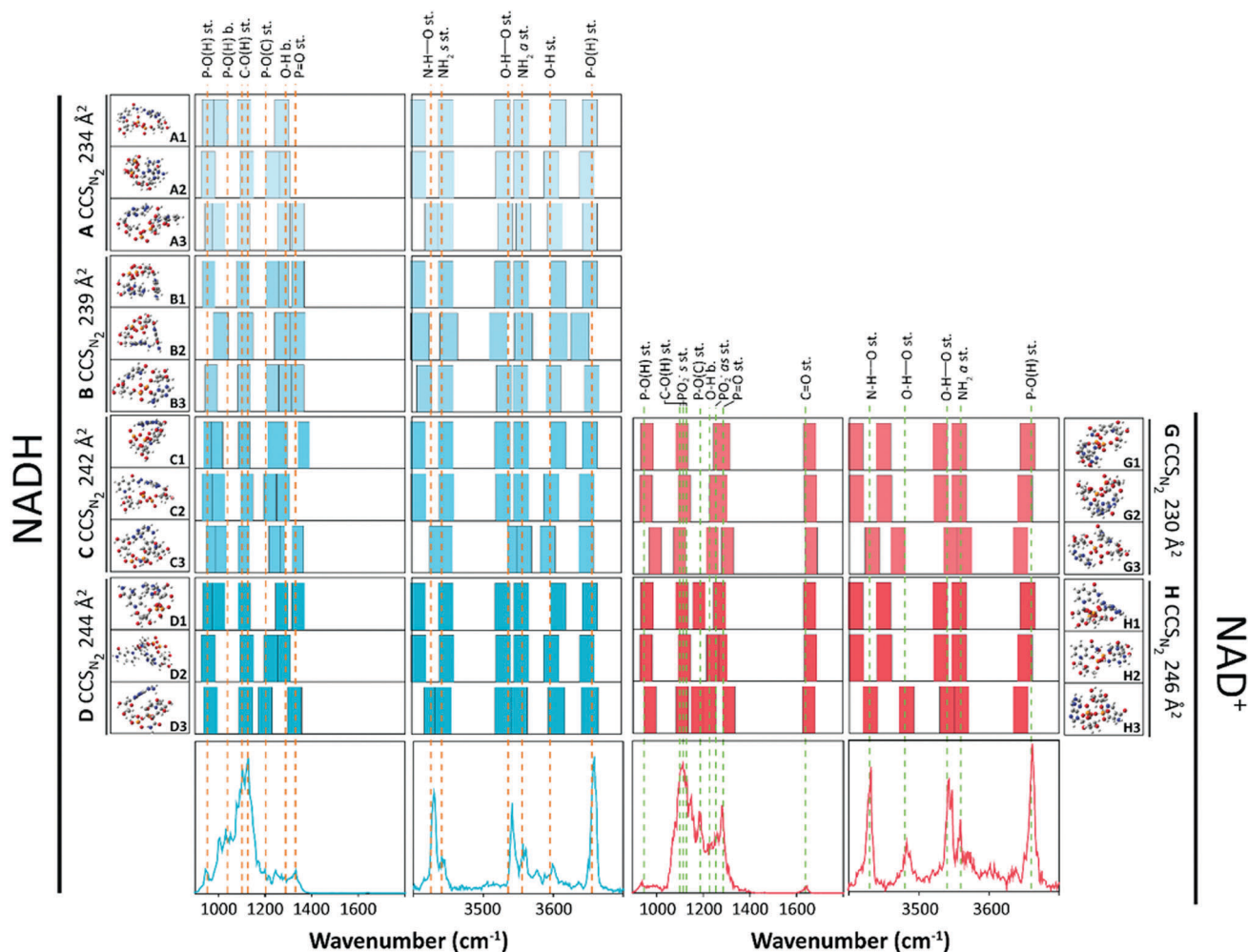

Fig. 5 Experimental and theoretical IRMPD spectra for the protonated NADH (blue) and NAD$^+$ (red) forms. The three lowest energy candidate structures per mobility band and corresponding IR spectra are shown. The boxes represent simplified calculated IR spectra to facilitate the visualization (complete calculated IR spectra are provided in Fig. S8, ESI†).

7048 | Phys. Chem. Chem. Phys., 2018, 20, 7043–7052

This journal is © the Owner Societies 2018

Clear evidence for changes in the hydrogen bonding network between NAD^+ and NADH could be observed in the OPO spectral range. While no band was observed in the case of NADH, a band at $\sim$3480 cm^{-1} was observed for NAD^+. The $\sim$3480 cm^{-1} band could be assigned to red-shifted alcohol OH stretches. This assignment was further supported by the differences in the infrared spectra of NAD^+ and NADH in the 800–1800 cm^{-1} spectral range. In fact, the P=O stretch band was red-shifted ($\sim$1290 cm^{-1}) for NAD^+, compared to NADH for where the corresponding band (1335 cm^{-1}) is typical of free P=O stretch and is indicative of the presence of an O–H–O stretch interaction (Fig. 5). In addition, the IRMPD spectra of NADH exhibited P–OH bend and stretch bands in the 900–1000 cm^{-1} spectral range, while these bands were observed with very low intensity in the case of NAD^+. Moreover, the IRMPD spectra of NAD^+ showed two signature bands at 1110 and 1255 cm^{-1}, not present in the case of NADH, corresponding to the PO_2^- symmetric and asymmetric stretches, respectively. That is, the P–OH stretch and P–OH bend bands in the IRMPD spectra of NADH suggest a non-zwitterionic form, while characteristic bands of PO_2^- asymmetric and symmetric stretches in the case of NAD^+ suggest that at least one of the phosphate groups is not protonated. In addition, a comparison between IRMPD and FTIR spectroscopy of NAD^+ in solution at low pH showed similar profiles in the 900–1300 cm^{-1} spectral range.[76] In fact, Nadolny and co-workers confirmed that the protonation of NAD^+ is located on the adenine residue (labeled N^9 in Fig. S9, ESI†) and that no additional proton is bound to the phosphate group with decreasing pH.

Further interpretation of the TIMS-MS and IRMPD spectra was assisted by the theoretical CCS_{N_2} and IR profiles from candidate structures obtained from molecular dynamics simulations (Fig. 5 and Tables S3, S4, ESI†). The selection of candidate structures was performed by comparing the three lowest energy candidates per IMS band observed (CCS_{N_2} within 5% error) and their calculated IR spectra. The candidate structures of the protonated NAD species can be grouped into three main conformational families: "close" (structures A and G in Fig. S2 and S6, ESI†), "stack" (peaks B and C in Fig. S3 and S4, ESI†), and "open" (peaks D and H in Fig. S5 and S7, ESI†). Note that the atoms in the structures of NAD^+ and NADH are numbered to facilitate the visualization of the intramolecular interactions (Fig. S9, ESI†). IRMPD spectra contain information about all the potential conformers, candidate structure assignment assumed that for each mobility band, the proposed structure can match most but not necessarily all the IRMPD bands.

Further inspection of the candidate structures revealed more details on the intramolecular interactions of the kinetically trapped intermediates species of NADH and NAD^+. In fact, theoretical calculations indicated intramolecular interactions involving N^2–H–O^{11} and O^5–H–O^{11} for the two common bands observed at $\sim$3430 and $\sim$3540 cm^{-1} (Fig. S10 and Tables S3–S6, ESI†). Furthermore, the characteristic band of NAD^+ observed near $\sim$3480 cm^{-1} is defined by an O^3–H–O^6 intramolecular interaction. Theoretical calculations of the candidate structures (Fig. S2–S7, ESI†) also showed common as well as signature

intramolecular interactions in both NADH and NAD^+ (Fig. S10 and Tables S5, S6, ESI†). For example, the O^6–H–O^{10}, O^6–H–O^{11}, O^6–H–N^9, N^8–H–O^{12} and O^4–H–O^6 intramolecular interactions appeared to be specific to NADH, while the N^2–H–O^5, O^5–H–N^7, O^6–H–N^7, N^2–H–O^6 and O^3–H–O^6 intramolecular interactions are involved in its NAD^+ form. In addition, this information allowed us to determine the specific intramolecular interactions involved in the three main conformational families (Fig. S11, ESI†). The O^6–H–O^{10} and N^2–H–O^6 intramolecular interactions appeared to be specific to the "closed" conformation, while the N^8–H–O^{12} and O^5–H–N^7 intramolecular interactions are specifically involved in the "stack" and "open" conformations, respectively. Common intramolecular interactions to the three conformational families are also highlighted implying O^1–H–N^8, O^5–H–O^{11} O^5–H–N^9, and N^2–H–O^{11} stretch interactions.

While IRMPD spectroscopy studies are only reported for the protonated forms of NAD, the comparison between the experimental and theoretical data of the sodiated species was limited to the CCS_{N_2} structural assignment. As for the protonated species, the lowest energy three candidate structures were selected per IMS band for the sodiated species (Fig. S12–S15 and Table S2, ESI†). Inspection of the candidate structures of the sodiated NAD species revealed that they can also be categorized in the three main conformational families: "close" (structures I, Fig. S14, ESI†), "stack" (structures E and J, Fig. S12 and S15, ESI†) and "open" (structures F, Fig. S13, ESI†). A detailed analysis of the sodiated candidate structures revealed the intramolecular interactions that stabilize the gas-phase ions (Fig. S16, ESI†). For example, the candidate structures for E and J bands indicated a parallel/antiparallel orientation between the nicotinamide and adenine moieties corresponding to the interactions between O^1–H–N^8, O^{10}–H–O^{12} and O^{11}–H–O^{12} maintaining the "stack" conformation; for all structures the most stable configurations corresponded to the metal position in the adenine group (Fig. S12 and S15, ESI†). The candidate structures for the I band showed a close interaction between the nicotinamide and adenine moieties involving intramolecular interactions between O^1–H–N^8, O^1–H–O^{10}, O^1–H–O^{11}, and O^6–H–O^{10} that stabilize the "close" conformation. In these interactions, the sodium cation is in proximity to the diphosphate group, instead of the adenine group, as observed in the "stack" conformers (Fig. S14, ESI†). For the candidate structures for the F band, the "open" conformations are stabilized by intramolecular interactions between O^5–H–O^{10} and O^5–H–O^{11}, where the main stabilization factor relies on the interactions between the members of the diphosphate group, while the sodium cation is located in the adenine group (Fig. S13, ESI†). While both sodiated NAD forms displayed a "stack" conformation, it appears that the "close" and "open" conformations are specific to the sodiated NAD^+ and NADH, respectively. In summary, the theoretical modelling suggests that the O^1–H–O^{10} and O^1–H–O^{11} intramolecular interactions appeared to be specific to the "close" conformation, while the O^{10}–H–O^{12}, O^{11}–H–O^{12} and O^5–H–O^{10}, O^5–H–O^{11} intramolecular interactions are specifically involved in the "stack" and "open" conformations, respectively.

While this information mostly reflects the findings made in the gas-phase (e.g., TIMS-MS and IRMPD experiments), it can

This journal is © the Owner Societies 2018

Phys. Chem. Chem. Phys., 2018, **20**, 7043–7052 | 7049

be extrapolated to better understand the possible mechanism that drive the conformational changes in solution, especially when memory effects of the solution conditions and similar trends to fluorescence lifetime spectroscopy and IRMPD were observed.

Conclusions

This work highlights an analytical workflow for complementary solution and gas-phase studies of biomolecules that utilizes fluorescence lifetime spectroscopy, trapped ion mobility spectrometry coupled to mass spectrometry (TIMS-MS), infrared multiple photon dissociation spectroscopy (IRMPD) and molecular dynamics simulations. The high resolving power of TIMS-MS permitted the separation of multiple IMS bands and retain the solvent ''memory'' as shown with the variation of the starting organic content. IRMPD permitted the assignment of intramolecular interactions and highlighted the main differences between the oxidized and reduced NAD forms. The IRMPD spectra of NADH suggest a non-zwitterionic form, while characteristic bands of PO_2^- symmetric and asymmetric stretches in the case of NAD^+ suggest that at least one of the phosphate groups is not protonated. For the first time, the intramolecular interactions that stabilize the conformational space of NAD^+ and NADH as well as the specific intramolecular interactions involved in the three main conformational families are described. The results obtained from the study of NAD in both solution and in the gas-phase, and the conformational exploration using molecular dynamics show that NAD^+ and NADH species can exist in ''open'', ''stack'', and ''closed'' conformations for both the protonated and sodiated forms, and that the driving force for the structural stability of each group and their conformational dynamics is hydrogen bonding. This work allows a better understanding of the structures involved in the biologically active NAD and could be used to parametrize and validate structure-based drug design approaches. This study highlights the need to further integrate TIMS-MS and IRMPD measurements in a single experiment to better differentiate the motifs that stabilize different mobility bands as suggested by others.[39,40]

Author contributions

The manuscript was written through contributions of all authors. All authors have given approval to the final version of the manuscript.

Funding sources

Conflicts of interest

The authors declare no competing financial interest.

Acknowledgements

References

1 M. Rossmann, *Nature*, 1976, **262**, 726.
2 P. Belenky, K. L. Bogan and C. Brenner, *Trends Biochem. Sci.*, 2007, **32**, 12–19.
3 V. Schreiber, F. Dantzer, J. C. Ame and G. de Murcia, *Nat. Rev. Mol. Cell Biol.*, 2006, **7**, 517–528.
4 H. H. Hassanain, S. Y. Chon and S. L. Gupta, *J. Biol. Chem.*, 1993, **268**, 5077–5084.
5 P. Bieganowski and C. Brenner, *Cell*, 2004, **117**, 495–502.
6 Q. Zhang, D. W. Piston and R. H. Goodman, *Science*, 2002, **295**, 1895–1897.
7 A. Wilkinson, J. Day and R. Bowater, *Mol. Microbiol.*, 2001, **40**, 1241–1248.
8 J. S. Smith and J. D. Boeke, *Genes Dev.*, 1997, **11**, 241–254.
9 J. Rutter, M. Reick, L. C. Wu and S. L. McKnight, *Science*, 2001, **293**, 510–514.
10 A. Burkle, *BioEssays*, 2001, **23**, 795–806.
11 R. M. Anderson, K. J. Bitterman, J. G. Wood, O. Medvedik, H. Cohen, S. S. Lin, J. K. Manchester, J. I. Gordon and D. A. Sinclair, *J. Biol. Chem.*, 2002, **277**, 18881–18890.
12 A. Katoh and T. Hashimoto, *Front. Biosci.*, 2004, **9**, 1577–1586.
13 N. Pollak, C. Dolle and M. Ziegler, *Biochem. J.*, 2007, **402**, 205–218.
14 J. Luo, A. Y. Nikolaev, S. Imai, D. Chen, F. Su, A. Shiloh, L. Guarente and W. Gu, *Cell*, 2001, **107**, 137–148.
15 H. Vaziri, S. K. Dessain, E. Ng Eaton, S. I. Imai, R. A. Frye, T. K. Pandita, L. Guarente and R. A. Weinberg, *Cell*, 2001, **107**, 149–159.
16 J. S. Smith, C. B. Brachmann, I. Celic, M. A. Kenna, S. Muhammad, V. J. Starai, J. L. Avalos, J. C. Escalante-Semerena, C. Grubmeyer, C. Wolberger and J. D. Boeke, *Proc. Natl. Acad. Sci. U. S. A.*, 2000, **97**, 6658–6663.
17 J. Landry, A. Sutton, S. T. Tafrov, R. C. Heller, J. Stebbins, L. Pillus and R. Sternglanz, *Proc. Natl. Acad. Sci. U. S. A.*, 2000, **97**, 5807–5811.
18 S. Imai, C. M. Armstrong, M. Kaeberlein and L. Guarente, *Nature*, 2000, **403**, 795–800.
19 S. J. Lin and L. Guarente, *Curr. Opin. Cell Biol.*, 2003, **15**, 241–246.

20 B. M. Bakker, K. M. Overkamp, A. J. van Maris, P. Kotter, M. A. Luttik, J. P. van Dijken and J. T. Pronk, *FEMS Microbiol. Rev.*, 2001, **25**, 15–37.

21 M. J. MacDonald and L. K. Marshall, *Arch. Biochem. Biophys.*, 2000, **384**, 143–153.

22 L. A. Sanni, C. Rae, A. Maitland, R. Stocker and N. H. Hunt, *Am. J. Pathol.*, 2001, **159**, 1105–1112.

23 R. Ramasamy, N. Trueblood and S. Schaefer, *Am. J. Physiol.*, 1998, **275**, H195–203.

24 P. D. Mongan, J. Capacchione, S. West, J. Karaian, D. Dubois, R. Keneally and P. Sharma, *Am. J. Physiol. Heart Circ. Physiol.*, 2002, **283**, H1634–1644.

25 A. Gaikwad, D. J. Long, 2nd, J. L. Stringer and A. K. Jaiswal, *J. Biol. Chem.*, 2001, **276**, 22559–22564.

26 J. M. Salmon, E. Kohen, P. Viallet, J. G. Hirschberg, A. W. Wouters, C. Kohen and B. Thorell, *Photochem. Photobiol.*, 1982, **36**, 585–593.

27 B. R. Masters, A. K. Ghosh, J. Wilson and F. M. Matschinsky, *Invest. Ophthalmol. Visual Sci.*, 1989, **30**, 861–868.

28 A. P. Koretsky, L. A. Katz and R. S. Balaban, *Am. J. Physiol.*, 1987, **253**, H856–862.

29 B. Chance and M. Lieberman, *Exp. Eye Res.*, 1978, **26**, 111–117.

30 D. M. Jameson, V. Thomas and D. M. Zhou, *Biochim. Biophys. Acta*, 1989, **994**, 187–190.

31 T. G. Scott, R. D. Spencer, N. J. Leonard and G. Weber, *J. Am. Chem. Soc.*, 1970, **92**, 687–695.

32 Y. D. Wu and K. N. Houk, *J. Am. Chem. Soc.*, 1991, **113**, 2353–2358.

33 J. J. Pavelites, J. Gao, P. A. Bash and A. D. Mackerell, *J. Comput. Chem.*, 1997, **18**, 221–239.

34 P. E. Smith and J. J. Tanner, *J. Mol. Recognit.*, 2000, **13**, 27–34.

35 J. C. Molano-Arevalo, D. R. Hernandez, W. G. Gonzalez, J. Miksovska, M. E. Ridgeway, M. A. Park and F. Fernandez-Lima, *Anal. Chem.*, 2014, **86**, 10223–10230.

36 E. R. Schenk, R. Almeida, J. Miksovska, M. E. Ridgeway, M. A. Park and F. Fernandez-Lima, *J. Am. Soc. Mass Spectrom*, 2015, **26**, 555–563.

37 E. R. Schenk, M. E. Ridgeway, M. A. Park, F. Leng and F. Fernandez-Lima, *Anal. Chem.*, 2014, **86**, 1210–1214.

38 E. R. Schenk, V. Mendez, J. T. Landrum, M. E. Ridgeway, M. A. Park and F. Fernandez-Lima, *Anal. Chem.*, 2014, **86**, 2019–2024.

39 O. Hernandez, S. Isenberg, V. Steinmetz, G. L. Glish and P. Maitre, *J. Phys. Chem. A*, 2015, **119**, 6057–6064.

40 A. Masson, M. Z. Kamrath, M. A. Perez, M. S. Glover, U. Rothlisberger, D. E. Clemmer and T. R. Rizzo, *J. Am. Soc. Mass Spectrom*, 2015, **26**, 1444–1454.

41 S. Lee, S. J. Valentine, J. P. Reilly and D. E. Clemmer, *Int. J. Mass Spectrom.*, 2012, **309**, 161–167.

42 S. Warnke, C. Baldauf, M. T. Bowers, K. Pagel and G. von Helden, *J. Am. Chem. Soc.*, 2014, **136**, 10308–10314.

43 N. C. Polfer, J. J. Valle, D. T. Moore, J. Oomens, J. R. Eyler and B. Bendiak, *Anal. Chem.*, 2006, **78**, 670–679.

44 J. S. Prell, T. M. Chang, J. A. Biles, G. Berden, J. Oomens and E. R. Williams, *J. Phys. Chem. A*, 2011, **115**, 2745–2751.

45 P. Kupser, K. Pagel, J. Oomens, N. Polfer, B. Koksch, G. Meijer and G. von Helden, *J. Am. Chem. Soc.*, 2010, **132**, 2085–2093.

46 R. J. Plowright, E. Gloaguen and M. Mons, *ChemPhysChem*, 2011, **12**, 1889–1899.

47 L. A. Flanagan, *U.S. Pat.*, No. 5872357 A, Hewlett-Packard Company, Palo Alto, CA, 1999, February 16, p. 19.

48 D. R. Hernandez, J. D. Debord, M. E. Ridgeway, D. A. Kaplan, M. A. Park and F. Fernandez-Lima, *Analyst*, 2014, **139**, 1913–1921.

49 F. A. Fernandez-Lima, D. A. Kaplan and M. A. Park, *Rev. Sci. Instrum.*, 2011, **82**, 126106.

50 F. A. Fernandez-Lima, D. A. Kaplan, J. Suetering and M. A. Park, *Int. J. Ion Mobility Spectrom.*, 2011, **14**, 93–98.

51 E. W. McDaniel and E. A. Mason, *Mobility and diffusion of ions in gases*, John Wiley and Sons, Inc., New York, New York, 1973.

52 R. D. Spencer, *J. Chem. Phys.*, 1970, **52**, 1654.

53 J. M. Beechem, *Chem. Phys. Lipids*, 1989, **50**, 237–251.

54 J. R. Lakowicz, *Principles of Fluorescence Spectroscopy*, Springer, New York, USA, 2010.

55 J. M. Bakker, T. Besson, J. Lemaire, D. Scuderi and P. Maitre, *J. Phys. Chem. A*, 2007, **111**, 13415–13424.

56 J. M. Bakker, R. K. Sinha, T. Besson, M. Brugnara, P. Tosi, J. Y. Salpin and P. Maitre, *J. Phys. Chem. A*, 2008, **112**, 12393–12400.

57 R. K. Sinha, E. Nicol, V. Steinmetz and P. Maitre, *J. Am. Soc. Mass Spectrom*, 2010, **21**, 758–772.

58 R. Prazeres, F. Glotin, C. Insa, D. A. Jaroszynski and J. M. Ortega, *Eur. Phys. J. D*, 1998, **3**, 87–93.

59 F. A. Fernandez-Lima, H. Wei, Y. Q. Gao and D. H. Russell, *J. Phys. Chem. A*, 2009, **113**, 8221–8234.

60 Y. Duan, C. Wu, S. Chowdhury, M. C. Lee, G. Xiong, W. Zhang, R. Yang, P. Cieplak, R. Luo, T. Lee, J. Caldwell, J. Wang and P. Kollman, *J. Comput. Chem.*, 2003, **24**, 1999–2012.

61 E. Krieger and G. Vriend, *Bioinformatics*, 2014, **30**, 2981–2982.

62 A. D. Bochevarov, E. Harder, T. F. Hughes, J. R. Greenwood, D. A. Braden, D. M. Philipp, D. Rinaldo, M. D. Halls, J. Zhang and R. A. Friesner, *Int. J. Quantum Chem.*, 2013, **113**, 2110–2142.

63 I. M. Alecu, J. Zheng, Y. Zhao and D. G. Truhlar, *J. Chem. Theory Comput.*, 2010, **6**, 2872–2887.

64 M. F. Mesleh, J. M. Hunter, A. A. Shvartsburg, G. C. Schatz and M. F. Jarrold, *J. Phys. Chem.*, 1996, **100**, 16082–16086.

65 A. A. Shvartsburg and M. F. Jarrold, *Chem. Phys. Lett.*, 1996, **261**, 86–91.

66 I. Campuzano, M. F. Bush, C. V. Robinson, C. Beaumont, K. Richardson, H. Kim and H. I. Kim, *Anal. Chem.*, 2011, **84**, 1026–1033.

67 C. Larriba and C. J. Hogan, *J. Comput. Phys.*, 2013, **251**, 344–363.

68 C. Larriba and C. J. Hogan, Jr., *J. Phys. Chem. A*, 2013, **117**, 3887–3901.

69 U. C. Singh and P. A. Kollman, *J. Comput. Chem.*, 1984, **5**, 129–145.

70 B. H. Besler, K. M. Merz and P. A. Kollman, *J. Comput. Chem.*, 1990, **11**, 431–439.

71 N. A. Pierson, S. J. Valentine and D. E. Clemmer, *J. Phys. Chem. B*, 2010, **114**, 7777–7783.

72 A. L. Patrick, C. N. Stedwell and N. C. Polfer, *Anal. Chem.*, 2014, **86**, 5547–5552.

73 T. N. Wassermann, O. V. Boyarkin, B. Paizs and T. R. Rizzo, *J. Am. Soc. Mass Spectrom*, 2012, **23**, 1029–1045.

74 E. E. Baquero, W. H. James, 3rd, S. H. Choi, S. H. Gellman and T. S. Zwier, *J. Am. Chem. Soc.*, 2008, **130**, 4784–4794.

75 K. Jeanne Dit Fouque, H. Lavanant, S. Zirah, V. Steinmetz, S. Rebuffat, P. Maitre and C. Afonso, *J. Phys. Chem. A*, 2016, **120**, 3810–3816.

76 C. Nadolny and G. Zundel, *J. Mol. Struct.*, 1996, **385**, 81–87.